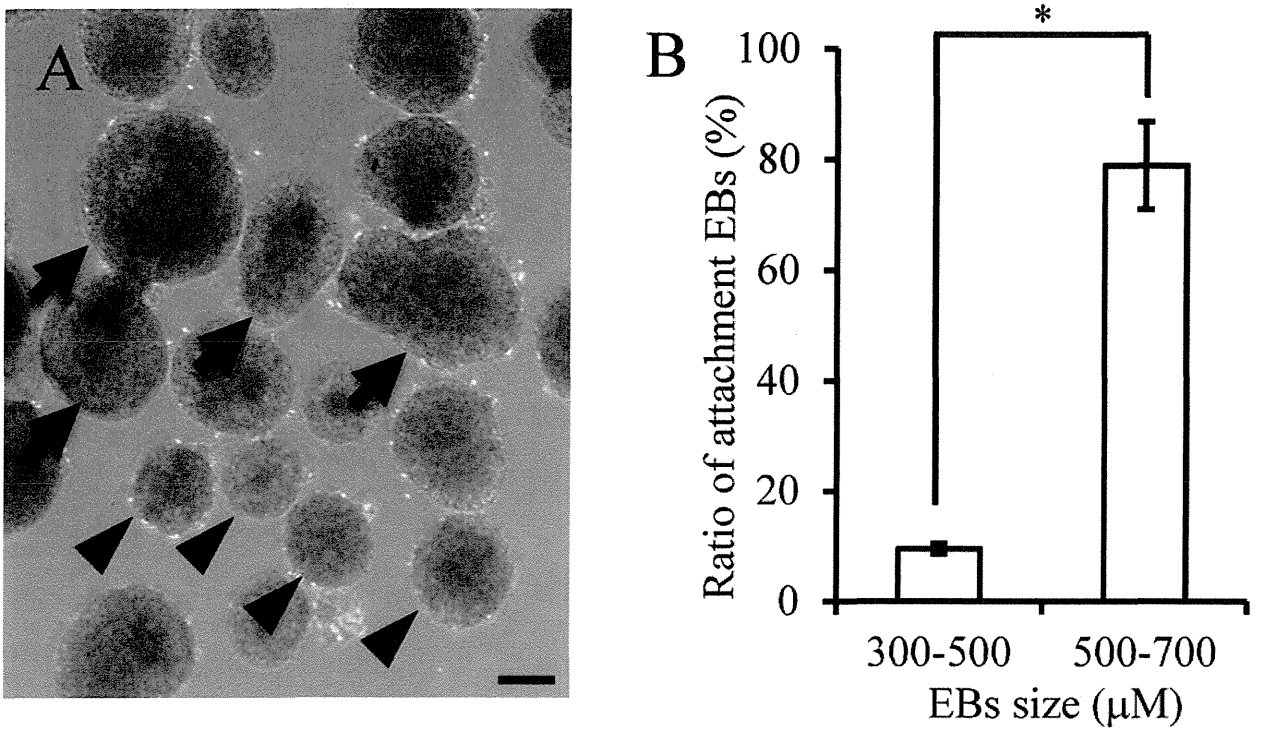


**Figure 3.** EB derived from the Fld-ES cell line. (A) Arrows indicate EB of 500 to 700 μm; arrowheads indicate EB of 300 to 500 μm. (B) The rates of attachment were 78.9% and 9.5% for EB of 500 to 700 μm and 300 to 500 μm, respectively. Data are expressed as means ± 1 SD. An asterisk indicates a significant ($P < 0.05$) difference. Scale bar, 200 μm.

culture of the EB derived from the Fld-ES and CMK6 cell lines, we confirmed their microtubular structure under the microscope. At the same time, we determined the neural cells in each colony through immunoassay of the 3 groups by using a confocal laser scanning microscope (Digital Eclipse C1, Nikon, Tokyo, Japan).

**Immunofluorescence microscopy.** Undifferentiated and differentiation-induced cells were fixed with 4% paraformaldehyde in PBS for 30 min. After permeabilization with 0.1% Triton X100 in PBS for 10 min and blocking with 3% BSA in PBS for 30 min, cells were incubated with primary antibodies overnight at 4 °C and visualized by using IgG or IgM conjugated with Alexa 488 or 555 (1:1000; Invitrogen). Primary antibodies for staining undifferentiated cells were Oct-3/4 (1:50; Becton Dickinson, Franklin Lakes, NJ); stage-specific embryonic antigen (SSEA) -1, -3, and -4; and tumor-related antigens (TRA)-1-60 and -1-81 (1:80; Chemicon). Primary antibodies for staining differentiated cells were β-tubulin III (1:200, Dako); glial fibrillary acidic protein (GFAP, 1:1000; Dako); and myelin basic protein (MBP, 1:1000; Dako). Nuclei were stained with Hoechst 33342 (10 μg/mL; Calbiochem, La Jolla, CA) in PBS and DAPI (1 μg/mL, 1:1000; Dako). Fluorescent images were produced by using a confocal laser scanning microscope (Digital Eclipse C1, Nikon).

## Results

**Establishment and characterization of the Fld-ES cell line.** We established the Fld-ES cell line from cynomolgus monkeys by using blastocysts with appropriate morphology that contained distinct, prominent inner cell masses. The morphology of these derived cells was very similar to that of other primate ES cells.[5,20] Finally, ES-like cells were generated in sufficient numbers to establish Fld-ES (Figure 1 A). This stable ES cell line did not require FGF2 supplementation to maintain an undifferentiated state during culture. However, we could not exclude the possibility that a small amount of FGF2 that might be derived from serum or feeder cells could have maintained the undifferentiated status of the ES cell line. Therefore, we putatively considered the cell line to be an FGF2 low-dose-dependent ES cell line.

We examined the karyotype and expression of undifferentiated markers in Fld-ES. Karyotyping analysis revealed that approximately 80% of cells examined after 18 passages had the normal chromosome number of 42, and the sex chromosomes were XY (Figure 1 B and C). Immunofluorescence revealed that Fld-ES strongly expressed Oct-3, SSEA-4, and TRA-1-60 and -1-81. ALP activity was observed, and SSEA-3 was expressed very weakly in some cells; no signals were observed for SSEA-1 (Table 1). To examine the pluripotency of Fld-ES, we induced the development of EB and teratomas in vivo (Figure 2). Immunohistochemical analysis revealed that ES cells transferred into 2 immunodeficient mice formed teratomas consisting of tissues from 3 embryonic germ layers (ectoderm, mesoderm, and endoderm; Figure 2 B through G).

**EB of different sizes have different attachment rates.** The rate of attachment on gelatin-coated dishes of EB of 500 to 700 μm in diameter (78.9%, 45 of 57) was higher than that of EB of 300 to 500 μm (9.5%, 6 of 63; Figure 3 A and B).

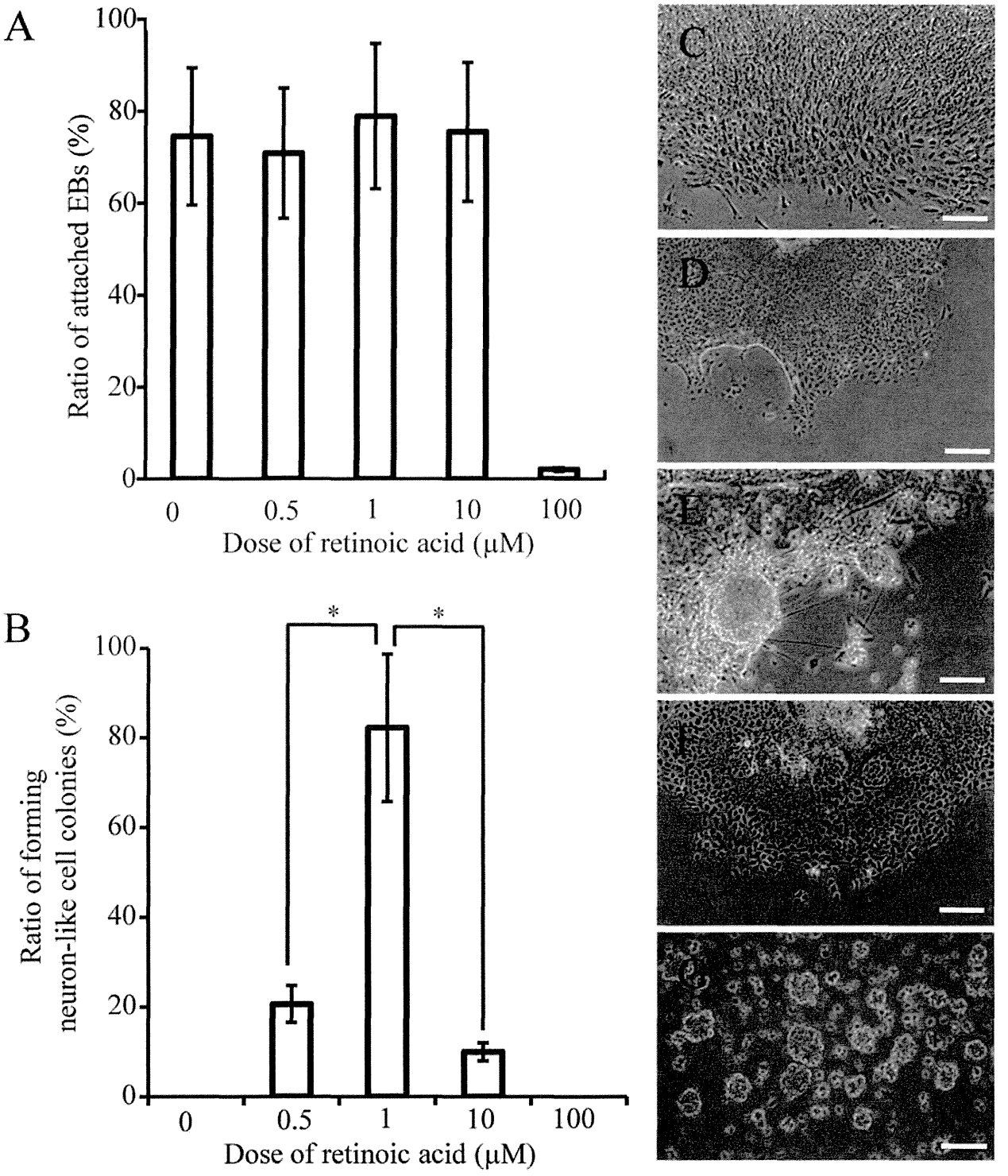


**Figure 4.** The attachment and neural differentiation ratio of EB derived from Fld-ES cells at each concentration of RA. (A) The ratio of attached EB on gelatin-treated dishes after the addition of retinoic acid at 4 concentrations. (B) The cells (except for the neural fibrillar structure) have extended like a sheet in the absence of retinoic acid. The colony with the structure of a microtubule was confirmed to have a high ratio of attached EB at 1 μM retinoic acid. The ratios of attached EB at 0.5 μM and 10 μM RA were low and that at 100 μM RA was negligible. The ES cells of all groups showed comparable results. (C through G) Colony formation at (C) 0, (D) 0.5, (E) 1, (F) 10, and (G) 100 μM retinoic acid. Scale bars, 200 μm. Data in panels A and B are expressed as means ± 1 SD. Asterisks in panel B indicate significant ($P < 0.05$) differences.

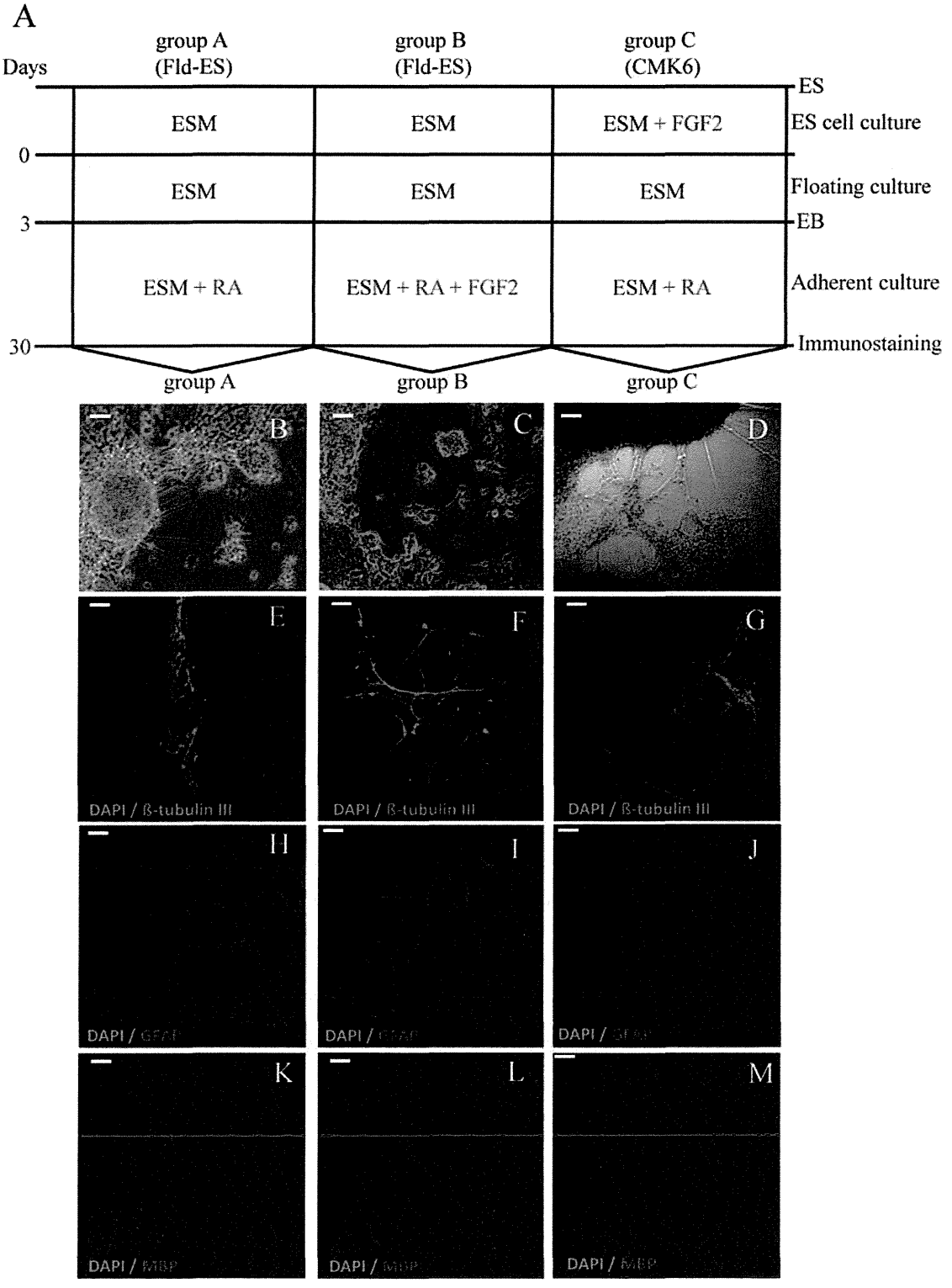


**Figure 5.** (A) Schematic illustration outlining the protocol for neural differentiation from Fld-ES and CMK6 cells. Groups A and B were Fld-ES cells cultured without added FGF2; group C was CMK6 cells cultured with FGF2. All groups formed EB after suspension cultures in ESM on untreated dishes for 3 d. EB were plated on gelatin-coated dishes at a density of 10 EB per dish. During this time, neural differentiation was induced by using RA only in groups A and C and both RA and FGF2 in group B. At 30 d after the initial formation of EB, neural cell markers were detected by immunostaining. (B–M) Morphologic changes in Fld-ES colonies after induction of neural differentiation and immunostaining analysis. (B–D) Nerve fibroid in clumps

**Dose-dependent effect of RA in EB differentiation.** During attempts to induce neural differentiation, we observed that 1 μM RA remarkably accelerated the development of microtubules (the ratio of microtubule formation was 84%) to a level comparable to that in Fld-ES cells along with a high attachment ratio, whereas 100 μM RA did not accelerate differentiation but showed a high dose effect (Figure 4 A through G). Accordingly, for differentiation of ES cells, we used ES cell medium supplemented with 1 μM RA for all 3 groups studied.

**Induction of neural differentiation in Fld-ES cells by RA and FGF2.** Neural differentiation was induced in Fld-ES and CMK6 cells in culture from attached EB according to the schedule shown in Figure 5 A. During differentiation, microtubules with cells that were beyond the attached EB colonies were present (Figure 5 B through D). We induced neural differentiation with RA and FGF2 in the medium from Fld-ES and CMK6 cells. While inducing differentiation of ES cells to neural cells after 10 d of culture (Figure 5 A), we confirmed the structure of the neuron fibers (Figure 5 B through D) emanating from the attached EB outgrowths in each defined culture. In the immunostaining analysis, adding only RA to the medium of Fld-ES and CMK6 cells resulted in microtubules positive for β-tubulin III (Figure 5 E and G). In addition, RA-treated Fld-ES cells were negative for GFAP (that is, astrocytes) whereas CMK6 cells were weakly positive (Figure 5 H and J); MBP staining for oligodendrocytes was negative in all groups (Figure 5 K and M). Combined treatment of Fld-ES cells with RA and FGF2 led to cells positive for both β-tubulin III and GFAP but negative for MBP (Figure 5 F, I, and L). Therefore, treatment of Fld-ES with only RA led primarily to the generation of microtubules positive for β-tubulin III, whereas treating Fld-ES cells with both FGF2 and RA induced the growth of large numbers of GFAP-expressing astrocytes that appeared outside of attached EB.

## Discussion

We established a cynomolgus monkey ES cell line that requires the addition of FGF2 to the medium for only 10 passages; after that, it can be maintained in an undifferentiated state without FGF2. This implies FGF2 low-dose dependence, and so we named the cell line Fld-ES. The Fld-ES cell line expresses primate ES-cell-specific markers, forms teratomas, and has a normal chromosome number,[20] suggesting that it is an important primate cell line for the study of the role of FGF2 during in vitro differentiation.

Before inducing in vitro differentiation, we observed that the attachment rate of EB formed from Fld-ES cells differed depending on their size: EB sizes of 500 to 700 μm had excellent adhesive capacity. Therefore, we used uniform EB of 500 to 700 μm, which showed strong adhesiveness, during neural differentiation. High-quality EB formation plays an important role in ES research for spontaneous differentiation into various cell types and even organ development.[3] Although specific reasons for the influence of size on EB adherence are unknown, perhaps larger EB have high numbers of functional cells that are important for attachment and subsequent differentiation.

Our findings regarding the concentration of RA in the differentiation of neural cells from Fld-ES were different from those in the mouse ES neural induction study.[3] The optimal concentration of RA to add to mouse ES cells to maximize the adhesiveness of EB was 0.5 μM,[4] whereas 1 μM RA had the best effect on neural differentiation in our monkey Fld-ES cell line. In mice, RA directly interacts with the retinoid receptor RAR/RXR and downregulates Wnt signaling to inhibit the mesodermal fate and adopt an ectodermal fate for neural differentiation.[15] We have demonstrated that the addition of RA to the culture medium of EB formed from Fld-ES cells made it possible for the cells to differentiate into neurons at 30 d after EB attachment began. In contrast, EB did not differentiate into astrocytes and oligodendrocytes. Moreover, the addition of both RA and FGF2 to the culture of EB from Fld-ES cells induced the differentiation of both neurons and astrocytes. We have not yet been able to induce oligodendrocytes from Fld-ES EB.

Another cynomolgus monkey ES cell line, CMK6, which was maintained in medium supplemented with FGF2, differentiated to neurons and a few astrocytes after the addition of RA only—that is, without an additional supply of FGF2 during differentiation. This difference may be due to the effect of FGF2, which was added to the medium of undifferentiating cultures before the start of the neural differentiation culture.

Because active RA signaling inhibits Wnt and Nodal signaling pathways to prevent the mesodermal fate of ES during differentiation into germ layer,[4] it can also stimulate the differentiation of neuroectodermal progenitor cells. However, the mechanisms of differentiation may differ among neurons, astrocytes, and oligodendrocytes derived from neuroectodermal progenitor cells, and perhaps RA enables the smooth induction of neurons. We also showed that the combined actions of RA and FGF2 yielded cultures containing both progenitor cells and neural cells, that is, both astrocytes and neurons. However, RA and FGF2 did not prompt oligodendrocyte induction at a specific step during the neural differentiation of cynomolgus monkey ES cells. Several researchers have reported that, in both mouse and primate pluripotent stem cells, inducing factors such as sonic hedgehog, noggin, and SB431542 regulate oligodendrocyte differentiation at different times by inhibiting BMP4/TGFβ and Activin/Nodal.[6,9,10] Therefore, oligodendrocyte differentiation seems to require specialized conditions and the presence of several factors at appropriate times.

In the present study, we established a novel monkey ES cell line that can maintain pluripotency without FGF2 supplementation of the culture medium. In addition, supplementation of our monkey Fld-ES line with both RA and FGF2 led to its differentiation to neural cells and astrocytes. The Fld-ES cell line may be useful for the study of neural differentiation-related signaling pathways.

---

of cells from all groups was confirmed after 10 d in suspension culture. (E–G) Expression of the neuron marker β-tubulin III (green) was confirmed in all groups. (H–J) Expression of the astrocyte marker GFAP (red) was confirmed in groups B and C but not in group A. In group B, Fld-ES-derived EB with added FGF2 demonstrated marked neural differentiation into astrocytes, whereas in group C, CMK6 cells cultured with FGF2 showed only weak differentiation into developing astrocytes. (K–M) Expression of the oligodendrocyte cell marker MBP (red) was not detected in any group. ESM, embryonic stem cell culture medium; FGF2, fibroblast growth factor 2; GFAP, glial fibrillary acidic protein; MBP, myelin basic protein; RA, retinoic acid. Scale bars, 50 μm.

## References


1. **Chambers SM, Fasano CA, Papapetrou EP, Tomishima M, Sadelain M, Studer L.** 2009. Highly efficient neural conversion of human ES and iPS cells by dual inhibition of SMAD signaling. Nat Biotechnol **27:**275–280.
2. **Chin MH, Mason MJ, Xie W, Volinia S, Singer M, Peterson C, Ambartsumyan G, Aimiuwu O, Richter L, Zhang J, Khvorostov I, Ott V, Grunstein M, Lavon N, Benvenisty N, Croce CM, Clark AT, Baxter T, Pyle AD, Teitell MA, Pelegrini M, Plath K, Lowry WE.** 2009. Induced pluripotent stem cells and embryonic stem cells are distinguished by gene expression signatures. Cell Stem Cell **5:**111–123.
3. **Choi YY, Chung BG, Lee DH, Khademhosseini A, Kim JH, Lee SH.** 2010. Controlled-size embryoid body formation in concave microwell arrays. Biomaterials **31:**4296–4303.
4. **Engberg N, Kahn M, Petersen DR, Hansson M, Serup P.** 2010. Retinoic acid synthesis promotes development of neural progenitors from mouse embryonic stem cells by suppressing endogenous, Wnt-dependent nodal signaling. Stem Cells **28:**1498–1509.
5. **Furuya M, Yasuchika K, Mizutani K, Yoshimura Y, Nakatsuji N, Suemori H.** 2003. Electroporation of cynomolgus monkey embryonic stem cells. Genesis **37:**180–187.
6. **Gil JE, Woo DH, Shim JH, Kim SE, You HJ, Park SH, Paek SH, Kim SK, Kim JH.** 2009. Vitronectin promotes oligodendrocyte differentiation during neurogenesis of human embryonic stem cells. FEBS Lett **583:**561–567.
7. **Honda A, Hirose M, Hatori M, Matoba S, Miyoshi H, Inoue K, Ogura A.** 2010. Generation of induced pluripotent stem cells in rabbits: potential experimental models for human regenerative medicine. J Biol Chem **285:**31362–31369.
8. **Honda A, Hirose M, Ogura A.** 2009. Basic FGF and activin/modal but not LIF signaling sustain undifferentiated status of rabbit embryonic stem cells. Exp Cell Res **315:**2033–2042.
9. **Izrael M, Zhang P, Kaufman R, Shinder V, Ella R, Amit M, Itskovitz-Eldor J, Chebath J, Revel M.** 2007. Human oligodendrocytes derived from embryonic stem cells: effect of noggin on phenotypic differentiation in vitro and on myelination in vivo. Mol Cell Neurosci **34:**310–323.
10. **Kim DS, Lee JS, Leem JW, Huh YJ, Kim JY, Kim HS, Park IH, Daley GQ, Hwang DY, Kim DW.** 2010. Robust enhancement of neural differentiation from human ES and iPS cells regardless of their innate difference in differentiation propensity. Stem Cell Rev **6:**270–281.
11. **Kim K, Doi A, Wen B, Ng K, Zhao R, Cahan P, Kim J, Aryee MJ, Ji H, Ehrlich LI, Yabuuchi A, Takeuchi A, Cunniff KC, Hongguang H, McKinney-Freeman S, Naveiras O, Yoon TJ, Irizarry RA, Jung N, Seita J, Hanna J, Murakami P, Jaenisch R, Weissleder R, Orkin SH, Weissman IL, Feinberg AP, Daley GQ.** 2010. Epigenetic memory in induced pluripotent stem cells. Nature **467:**285–290.
12. **Koch P, Opitz T, Steinbeck JA, Ladewig J, Brüstle O.** 2009. A rosette-type, self-renewing human ES cell-derived neural stem cell with potential for in vitro instruction and synaptic integration. Proc Natl Acad Sci USA **106:**3225–3230.
13. **Li XJ, Hu BY, Jones SA, Zhang YS, Lavaute T, Du ZW, Zhang SC.** 2008. Directed differentiation of ventral spinal progenitors and motor neurons from human embryonic stem cells by small molecules. Stem Cells **26:**886–893.
14. **Niwa H, Ogawa K, Shimosato D, Adachi K.** 2009. A parallel circuit of LIF signalling pathways maintains pluripotency of mouse ES cells. Nature **460:**118–122.
15. **Okada Y, Shimazaki T, Sobue G, Okano H.** 2004. Retinoic-acid-concentration-dependent acquisition of neural cell identity during in vitro differentiation of mouse embryonic stem cells. Dev Biol **275:**124–142.
16. **Patani R, Compston A, Puddifoot CA, Wyllie DJ, Hardingham GE, Allen ND, Chandran S.** 2009. Activin/nodal inhibition alone accelerates highly efficient neural conversion from human embryonic stem cells and imposes a caudal positional identity. PLoS ONE **4:**e7327.
17. **Polo JM, Liu S, Figueroa ME, Kulalert W, Eminli S, Tan KY, Apostolou E, Stadtfeld M, Li Y, Shioda T, Natesan S, Wagers AJ, Melnick A, Evans T, Hochedlinger K.** 2010. Cell type of origin influences the molecular and functional properties of mouse induced pluripotent stem cells. Nat Biotechnol **28:**848–855.
18. **Reubinoff BE, Pera MF, Fong CY, Trounson A, Bongso A.** 2000. Embryonic stem cell lines from human blastocysts: somatic differentiation in vitro. Nat Biotechnol **18:**399–404.
19. **Shimozawa N, Nakamura S, Takahashi I, Hatori M, Sankai T.** 2010. Characterization of a novel embryonic stem cell line from an intracytoplasmic sperm injection-derived blastocyst in the African green monkey. Reproduction **139:**565–573.
20. **Suemori H, Tada T, Torii R, Hosoi Y, Kobayashi K, Imahie H, Kondo Y, Iritani A, Nakatsuji N.** 2001. Establishment of embryonic stem cell lines from cynomolgus monkey blastocysts produced by IVF or ICSI. Dev Dyn **222:**273–279.
21. **Sumi T, Tsuneyoshi N, Nakatsuji N, Suemori H.** 2008. Defining early lineage specification of human embryonic stem cells by the orchestrated balance of canonical Wnt/β-catenin, activin/nodal, and BMP signaling. Development **135:**2969–2979.
22. **Terashima M, Kobayashi M, Motomiya M, Inoue N, Yoshida T, Okano H, Iwasaki N, Minami A, Matsuoka I.** 2010. Analysis of the expression and function of BRINP family genes during neuronal differentiation in mouse embryonic stem cell-derived neural stem cells. J Neurosci Res **88:**1387–1393.
23. **Thomson JA, Itskovitz-Eldor J, Shapiro SS, Waknitz MA, Swiergiel JJ, Marshall VS, Jones JM.** 1998. Embryonic stem cell lines derived from human blastocysts. Science **282:**1145–1147.
24. **Thomson JA, Kalishman J, Golos TG, Durning M, Harris CP, Becker RA, Hearn JP.** 1995. Isolation of a primate embryonic stem cell line. Proc Natl Acad Sci USA **92:**7844–7848.
25. **Thomson JA, Kalishman J, Golos TG, Durning M, Harris CP, Hearn JP.** 1996. Pluripotent cell lines derived from common marmoset (*Callithrix jacchus*) blastocysts. Biol Reprod **55:**254–259.
26. **Tonge PD, Andrews PW.** 2010. Retinoic acid directs neuronal differentiation of human pluripotent stem cell lines in a non-cell-autonomous manner. Differentiation **80:**20–30.
27. **Wada T, Honda M, Minami I, Tooi N, Amagai Y, Nakatsuji N, Aiba K.** 2009. Highly efficient differentiation and enrichment of spinal motor neurons derived from human and monkey embryonic stem cells. PLoS ONE **4:**e6722.
28. **Zhang X, Wang S, Yang S, Li T, Ji S, Chen H, Li B, Jin L, Xie Y, Hu Z, Chi J.** 2006. Feeder layer and serum-free culture of rhesus monkey embryonic stem cells. Reprod Biomed Online **13:**412–420.
29. **Zhou J, Su P, Li D, Tsang S, Duan E, Wang F.** 2010. High-efficiency induction of neural conversion in human ESCs and human induced pluripotent stem cells with a single chemical inhibitor of transforming growth factor βsuperfamily receptors. Stem Cells **28:**1741–1750.

# Cardiopulmonary Bypass Induces Recruitment of Bone Marrow–Derived Leukocytes to the Lungs in Monkeys

Yukinobu Goto, MD, PhD, Yuji Hiramatsu, MD, PhD, Naohide Ageyama, DVM, PhD, Shoko Sato, BMT, Shinya Kanemoto, MD, PhD, Yukio Sato, MD, PhD, and Yuzuru Sakakibara, MD, PhD

Departments of Thoracic Surgery and Cardiovascular Surgery, Faculty of Medicine, University of Tsukuba, and Tsukuba Primate Research Center, National Institute of Biomedical Innovation, Tsukuba, Japan

*Background.* A bone marrow (BM) response induced by cardiopulmonary bypass (CPB) as a systemic inflammatory reaction has previously been postulated but not clarified. Newly released polymorphonuclear leukocytes (PMNs) and monocytes from the BM are known to be immature, indicating their greater potential to damage tissue. The present study aimed to examine the kinetics of BM-derived leukocytes associated with CPB in a nonhuman primate model.

*Methods.* Normothermic CPB was performed in cynomolgus monkeys for 2 hours through a median sternotomy. Leukocyte precursors were labeled in the BM of the monkeys in vivo by an intravenous injection of 5-bromo-2′-deoxyuridine (BrdU), and their release into the circulation and recruitment to the lungs after operation with or without CPB (control group) were monitored over time by flow cytometry.

*Results.* In normal-state monkeys, the calculated transit time of BrdU-labeled PMNs ($PMN^{BrdU}$) through the BM was 143.6 ± 4.5 hours and that of monocytes was 100.9 ± 7.6 hours. CPB caused a rapid release of PMNs and monocytes from the BM, shortened their transit through the BM to 92.0 ± 4.1 and 60.3 ± 2.9 hours, respectively, and further induced their increased appearance in the alveolar spaces, with a significant increase in both interleukin (IL)-6 and IL-8 levels in the bronchoalveolar lavage fluid (BALF) 24 hours after CPB.

*Conclusions.* CPB accelerated the release of PMNs and monocytes from the BM and their recruitment to the lungs in our monkey model, indicating that this model is relevant for monitoring the kinetics of BM-derived leukocytes in humans.

(Ann Thorac Surg 2014;97:617–23)


We previously demonstrated the activation of circulating polymorphonuclear leukocytes (PMNs) or monocytes during cardiopulmonary bypass (CPB) in vitro using a simulated CPB model [1, 2]. Accumulation and migration of these leukocytes from the circulation to the lungs after CPB have the potential to amplify inflammatory reactions and lung injury [3, 4]. However, the effects of hemodilution, ischemia-reperfusion, and new cells being recruited are not factored into in vitro CPB models, including our own. Some animal models that were developed to clarify the in vivo pathophysiologic processes of this life-threatening condition indicated that leukocyte production by the bone marrow (BM) can be stimulated by CPB [3]. More than 95% of leukocytes are found in the BM, including in the mitotic, maturation, and storage pools; 3% are found in the marginated pool adhering to the endothelium; and 2% are found in the circulating blood [5]. Given this distribution of leukocytes, those that accumulate in the lungs as a result of CPB originate not only from the circulation but also from new cells released from the BM. Although sequestration of circulating leukocytes to the lungs is known to be activated by contact with the artificial circuit surfaces of the CPB apparatus, the mechanism by which CPB affects the BM in vivo, especially the kinetics of BM-derived leukocytes after CBP, has scarcely been studied.

In the present study, we focused on these BM-derived leukocytes and investigated their recruitment to the lungs using our established primate CPB model. The thymidine analogue 5-bromo-2′-deoxyuridine (BrdU) was used to label dividing leukocytes in the BM [6] and to follow their release into the circulation and recruitment to the lungs, which were identified by flow cytometric analysis. We hypothesized that the behavior of BM-derived leukocytes after CPB plays an important role in the pathogenesis of lung injury after CPB. To the best of our knowledge, this is the first systematic study of the BM reaction over time associated with CPB using a primate model.

Accepted for publication Oct 22, 2013.

Address correspondence to Dr Goto, Department of Thoracic Surgery, Faculty of Medicine, University of Tsukuba, 1-1-1 Tennodai, Tsukuba 305-8575, Japan; e-mail: ygoto@md.tsukuba.ac.jp.


Published by Elsevier Inc

0003-4975/$36.00
http://dx.doi.org/10.1016/j.athoracsur.2013.10.072

## Material and Methods

### *Animals*

Male cynomolgus monkeys (*Macaca fascicularis*) (n = 14; 4–6 years old, 4.9 ± 0.4 kg) born in the Tsukuba Primate Center were used as the nonhuman primate model. The protocol was approved by the Animal Welfare and Animal Care Committee of the National Institute of Infectious Diseases (Tokyo, Japan) and by the Animal Experimentation Committee of the University of Tsukuba. The study strictly adhered to the Rules for Animal Care and Management of the Tsukuba Primate Center [7] and to the Guiding Principles for Animal Experiments Using Nonhuman Primates formulated by the Primate Society of Japan [8].

### *Monkey Model of CPB*

The monkeys were anesthetized with ketamine hydrochloride (Ketalar, 10 mg/kg; Sankyo, Tokyo, Japan) and xylazine hydrochloride (Seraktar, 0.5 mg/kg; Bayer, Leverkusen, Germany) followed by inhaled isoflurane (5% for induction and 2% for maintenance). After induction of anesthesia, the monkeys underwent endotracheal intubation and ventilation with a respirator (A.D.S. 1000; Shin Ei Industries, Saitama, Japan). The left femoral artery was then isolated and catheterized (20-gauge catheter) for monitoring arterial pressure. Rectal temperature (kept at 37°C during CPB) was monitored throughout the anesthesia procedure. CPB was established with an ascending aorta cannula (12F) for arterial inflow, and superior (10F) and inferior (10F) venae cavae cannulation for venous outflow after systemic heparinization (250 U/kg). The circuit for the CPB was assembled with polytetrafluoroethylene tubing (Mera Exceline; Senko Medical Instrument, Tokyo, Japan), incorporating an infant-type membrane oxygenator (HPO-06RHF-C; Senko Medical Instrument), an arterial filter (HAF-C1; Senko Medical Instrument), and a roller pump (HAD-11; Senko Medical Instrument). The pump prime consisted of approximately 200 mL of Ringer's acetate solution and 75 mL of autologous blood (harvested at 25 mL/week for 3 weeks before the operation) with acid-citrate-dextrose to achieve a hematocrit level of 20%. Normothermic CPB was started at a flow rate of 120 mL/kg/min, and perfusion without cardiac arrest was maintained for 120 minutes in total. To establish 30 minutes of pulmonary ischemia at 30 minutes after the initiation of CPB, additional tapes were placed around the venae cavae and passed through small tubing so that they could be cinched down as tourniquets or snares around the cannula, thereby forcing all the venous return to pass out into the CPB, preventing any systemic venous blood from getting into the right side of the heart. The activated clotting time was greater than 400 seconds throughout perfusion. The monkey was weaned from CPB and protamine sulfate was given to neutralize the heparin at a ratio of 1:1. After satisfactory hemostasis was ensured, the sternum was closed. The total amount of blood withdrawn was limited to less than 10% of the monkey's body weight, and blood remaining in the extracorporeal circuit was reinfused at the end of the CPB.

### *Experimental Design*

CPB was performed on 5 monkeys for 2 hours through a median sternotomy. For the control group, monkeys (n = 4) underwent only sternotomy under general anesthesia. To label dividing cells in the BM, BrdU (100 mg/kg; Sigma-Aldrich, St. Louis, MO) was intravenously infused 24 hours before the operation. This time point was selected because in our preliminary study, the first BrdU-labeled PMN ($PMN^{BrdU}$) appeared in the circulation 24 hours after BrdU administration (n = 5 ) (Fig 1). After the procedure, the monkeys were allowed to recover, and the peripheral blood samples were obtained just before (time 0) and at intervals from 24 to 192 hours after the BrdU injection. Total white blood cell (WBC) counts were determined with a model Sysmex KX-21 (Sysmex, Kobe, Japan) and the number of $PMN^{BrdU}$ and BrdU-labeled monocytes ($MO^{BrdU}$) included was determined by flow cytometric assay as described further on. Differential WBC counts were obtained by counting 200 leukocytes in randomly selected fields of view on Wright-Giemsa–stained blood smears. Bronchoalveolar lavage fluid (BALF) samples were also collected at the same time points for monitoring BrdU-labeled leukocyte recruitment to the lungs. Briefly, after anesthesia induction at each time point, the primates were intubated, and a flexible 10F soft catheter (SF-ND1013OS; Terumo, Tokyo, Japan) connected to a specimen collection container (2586-M, Argyle; Covidien, Shizuoka, Japan) was inserted through an inline adapter in the anesthesia breathing circuit. The catheter was advanced into the lung and wedged in the bronchus. Sterile saline (10 mL) was instilled and aspirated through the catheter. BALF recovery in the container was typically 60% of the instilled volume. Total nucleated cell counts were obtained for each sample. BALF was filtered through a 42-μm nylon mesh and then centrifuged. The supernatants were removed and cells were resuspended with phosphate-buffered saline for flow cytometry, as described further on. Cytokine levels of interleukin (IL)-6 (Invitrogen/Life Technologies, Grand Island, NY) and IL-8 (Abnova, Taipei City, Taiwan) in these supernatants were measured at 24, 48, and 72 hours after the BrdU injection by enzyme-linked immunosorbent assay according to the manufacturer's instructions.

### *Flow Cytometric Analysis*

BrdU-positive PMNs and monocytes in the peripheral blood and BALF samples were determined by 2-color immunofluorescent flow cytometric analysis. One hundred microliters of whole blood in ethylenediaminetetraacetic acid and a cell suspension from the BALF were stained with the peridinin-chlorophyll protein–conjugated mononuclear antibody and CD14 (mouse antihuman CD14 mAb Tuk4; Miltenyi Biotec, Tokyo, Japan), followed by fluorescein isothiocyanate (FITC)-conjugated monoclonal mouse anti-BrdU antibody after a preparation of a commercially available kit, BrdU Flow Kit (BD Biosciences, San Jose, CA). Mononuclear cells were recognized in the flow cytometer (FACSCalibur

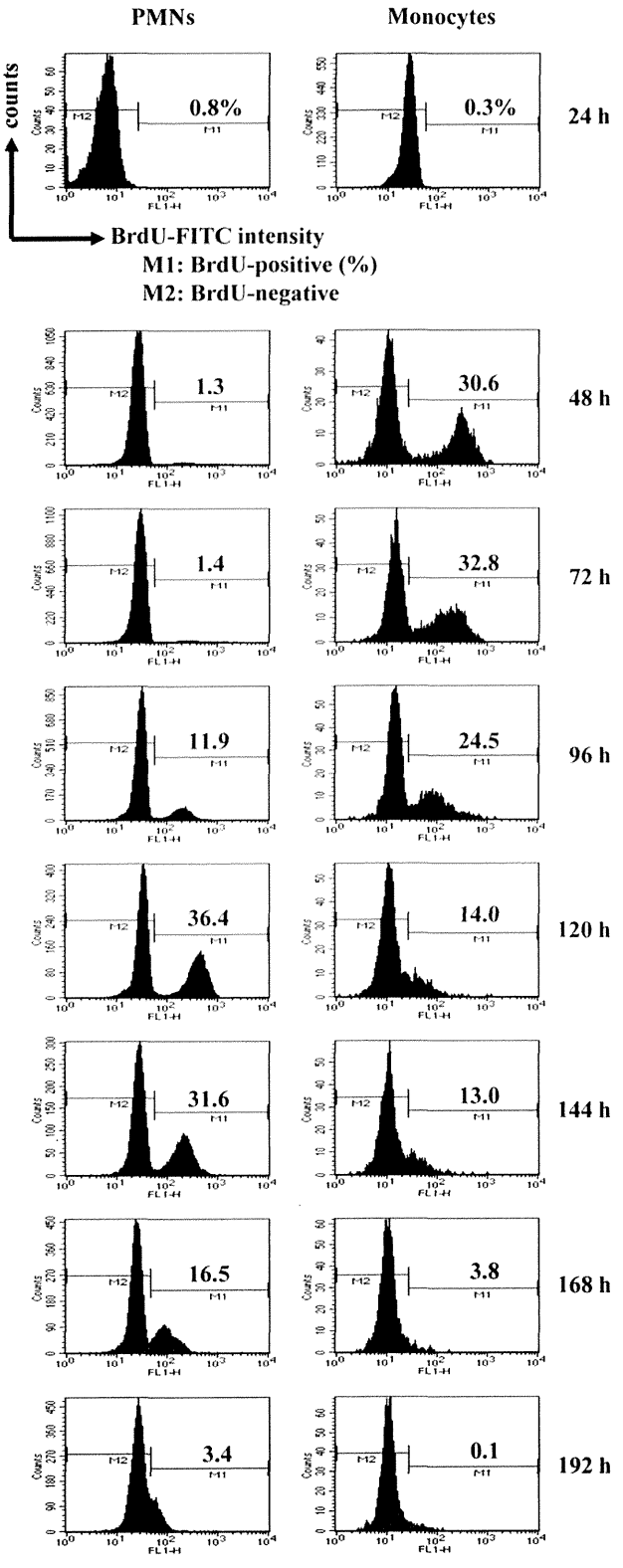


*Fig 1. Typical temporal histogram changes in circulating 5-bromo-2′-deoxyuridine (BrdU)-labeled polymorphonuclear leukocytes ($PMN^{BrdU}$) (left side of figure) and BrdU-labeled monocytes ($MO^{BrdU}$) (right side of figure) from 1 monkey are shown. In each histogram, BrdU-positive cells were recognized by their high fluorescein isothiocyanate (FITC) fluorescence intensity, which is indicated as region M1 (BrdU-negative cells are indicated as region M2) and expressed as percentage of cells that were BrdU-labeled. First $PMN^{BrdU}$ appeared in the circulation 24 hours after BrdU labeling and then gradually increased before reaching peak at 120 hours (32.3% ± 5.8%; means ± standard deviation [SE] obtained for 5 monkeys); thereafter they declined. The peak for $MO^{BrdU}$ occurred at 72 hours (27.7% ± 2.7%), which was much earlier than that for $PMN^{BrdU}$ ($P = 0.005$).*

using BD CellQuest Pro software; Becton, Dickinson, Tokyo, Japan) by gating out PMNs that were identified according to the typical forward and side scatter pattern. Monocytes were then distinguished on the basis of positive expression of CD14 as indicated by high peridinin-chlorophyll fluorescence intensity. A total of 3,000 cells per specimen were evaluated, and results were expressed as the percentage of $PMN^{BrdU}$ or $MO^{BrdU}$, which were recognized by their high FITC fluorescence intensity. The transit times of the leukocytes through the BM were calculated as described elsewhere [6].

### *Statistical Analysis*

Data were expressed as means ± standard error (SE). The results were analyzed using a repeated-measure analysis of variance over time in which the effect of multiple comparisons was corrected using the Bonferroni method (PASW Statistics, version 18.0 for Windows; SPSS, Chicago, IL). The transit time of PMNs or monocytes was compared by 1-way analysis of variance, followed by a post hoc Tukey's test among the groups. Differences were considered significant when $p$ was less than 0.05.

## Results

### *Flow-Cytometric Detection of BrdU-Labeled Leukocytes in the Circulation in Monkeys*

Fig 1 shows typical histograms of flow cytometric analysis of the appearance of $PMN^{BrdU}$ and $MO^{BrdU}$ in the circulation over time after labeling with BrdU. The changes in these histograms obtained for 5 monkeys and the calculated mean transit time of $PMN^{BrdU}$ through the BM in normal-state monkeys was 143.6 ± 4.5 hours, which was much longer than the values obtained for monocytes (100.9 ± 7.6 hours) ($p = 0.018$) (Table 1).

### *Kinetics of BM-Derived Leukocytes After CPB*

Leukocyte numbers were corrected by using the hematocrit values for significant dilution after CPB. Changes in the circulating PMN and monocyte counts during the protocol did not differ significantly between the CPB group and the control group (Fig 2A). The mean leukocyte counts were significantly increased after CPB when compared with those before CPB ($p = 0.042$). However, the proportions of this increase in leukocyte counts after CPB did not differ significantly between the groups. In contrast, a significantly larger number of nucleated cells in the alveolar spaces were found in the CPB group

Ann Thorac Surg
2014;97:617–23



*Table 1. Transit Times of Leukocytes Through the Bone Marrow*

| Group (n) | PMNs (h) | Monocytes (h) |
|---|---|---|
| Surgical procedure | | |
| With CPB (5) | 92.0 ± 4.1[a] | 60.3 ± 2.9[a] |
| Without CPB (controls) (4) | 123.6 ± 9.0 | 93.2 ± 2.5 |
| No operation (5) | 143.6 ± 4.5[b] | 100.9 ± 7.6 |

[a] $P < 0.05$ versus control group. [b] $P < 0.02$ versus monocytes.

All values represent the means ± SE.

CPB = cardiopulmonary bypass.

(with a peak at 48 hours) compared with that in the control group (Fig 2B).

The percentages of $PMN^{BrdU}$ or $MO^{BrdU}$ in the circulation of the monkeys after the surgical procedure, with or without CPB (control group), are shown in Figs 3A and 3B. The appearance of $PMN^{BrdU}$ (with a peak at 96 hours) and $MO^{BrdU}$ (with a peak at 48 hours) in the circulation of the CPB group was significantly earlier than in the controls. The calculated transit times of $PMN^{BrdU}$ and $MO^{BrdU}$ through the BM were significantly shorter in the CPB group than in the control group (92.0 ± 4.1 hours versus 123.6 ± 9.0 hours; $p = 0.038$ and 60.3 ± 2.9 hours versus 93.2 ± 2.5 hours; $p = 0.041$, respectively) (Table 1).

Fig 4 shows the absolute number of BrdU-labeled cells in the BALF after the surgical procedure with or without CPB (control group). The values in the control group increased gradually over time, whereas CPB caused a significant increase in these cells within 24 hours of CPB compared with the control group, reaching a peak at 96 hours after CPB ($p = 0.033$). The percentages of the $PMN^{BrdU}$ contained in these cells in the BALF was 51.5% ± 8.0% at 24 hours and 65.8% ± 7.4% at 96 hours after CPB. CPB also induced a significant increase in both IL-6 (Fig 5A) and IL-8 (Fig 5B) levels in the BALF at 48 hours (24 hours after CPB) compared with the control monkeys (66.2 ± 27.7 U/mL versus 15.5 ± 2.6 U/mL; $p = 0.028$ and 1444.2 ± 500.7 U/mL versus 512.6 ± 278.8 U/mL; $p = 0.042$, respectively).

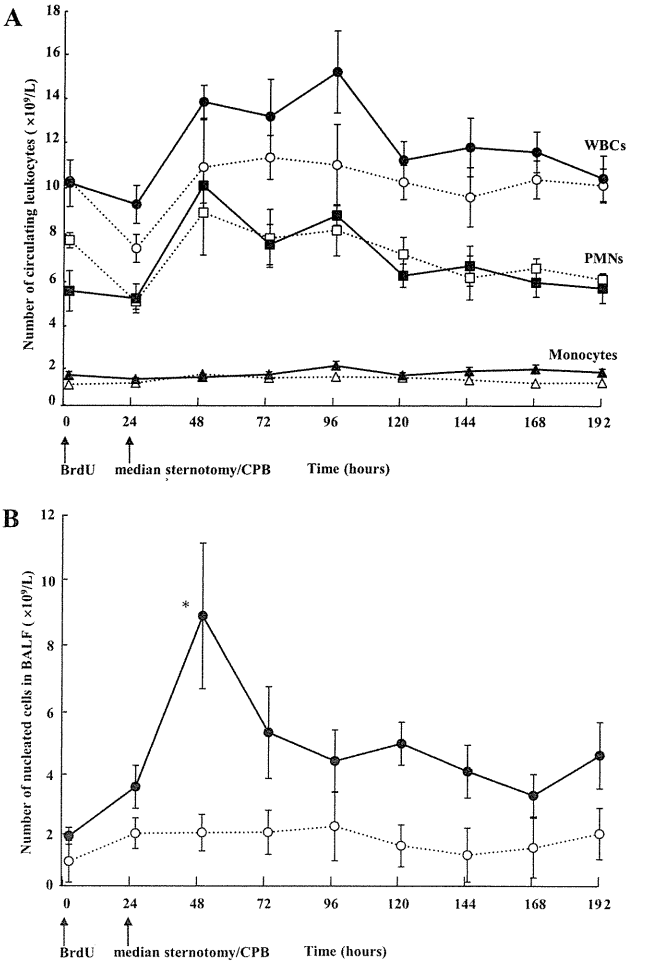


*Fig 2. Changes in counts of (A) circulating white blood cells (WBCs), polymorphonuclear leukocytes (PMNs), and monocytes and (B) nucleated cells in the bronchoalveolar lavage fluid (BALF) after cardiopulmonary bypass (CPB) (solid line: n = 5) and in control group (dashed line: n = 4). Changes in circulating WBCs, PMNs, and monocytes did not differ between groups. In contrast, number of cells in alveolar spaces of lung was increased in the CPB group (with peak at 48 hours). Each value represents mean ± standard error (SE). *P < 0.05 versus control group. (BrdU = 5-bromo-2′-deoxyuridine.)*

## Comment

Our results showing that CPB induces a greater appearance of cells in the alveolar spaces (with a peak at 24 hours after CPB) is consistent with the findings of previous reports [3, 4]. Our data also extend this observation by showing that the number of BM-derived leukocytes in the alveolar spaces was elevated and reached a peak at 96 hours rather than at 24 hours after CPB. Previous studies have shown that these newly released PMNs and monocytes from the BM are immature, because the maturation process in the marrow has been shortened [6, 9]. These immature leukocytes then preferentially sequester to the lung [9, 10], which has been attributed to their size and a decrease in their deformability. Moreover, PMNs migrate less efficiently into the alveolar spaces than do their mature counterparts, indicating their greater potential to damage tissue. Our results indicate that when the number of BM-derived cells reached its peak (96 hours) after CPB, PMNs remained the majority (65.8%) of these recruited cells in the alveolar spaces. These results strongly suggest that this delayed recruitment of BM-derived PMNs after CPB plays an important role in the pathogenesis of lung injury after CPB. This suggestion is supported by a common clinical finding that most patients who do not have any pulmonary dysfunction right after CPB experience significant respiratory impairment a couple of days after the operation [3, 4].

Previous studies reported that elevated plasma levels of tumor necrosis factor-α, IL-6, and IL-8, in turn, were strongly correlated with postoperative pulmonary dysfunction and prolonged intubation [11]. Our data

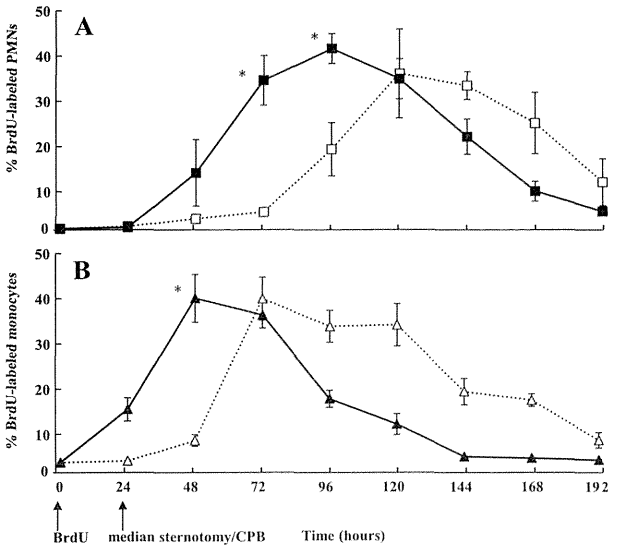


Number of BrdU-labeled PMNs ($\times 10^7$/L)

| | | | | | | | | |
|---|---|---|---|---|---|---|---|---|
| CPB : | 11.5 | 122.8 | 268.7 | 311.3 | 213.4 | 141.9 | 53.8 | 22.2 |
| Control : | 11.8 | 26.6 | 32.3 | 163.0 | 238.0 | 204.1 | 151.6 | 62.2 |

Number of BrdU-labeled monocytes ($\times 10^7$/L)

| | | | | | | | | |
|---|---|---|---|---|---|---|---|---|
| CPB : | 27.8 | 82.2 | 76.3 | 47.3 | 39.0 | 6.4 | 5.4 | 2.7 |
| Control : | 5.7 | 21.1 | 76.6 | 63.2 | 70.0 | 43.7 | 28.0 | 13.0 |

*Fig 3. Percentages of circulating (A) 5-bromo-2′-deoxyuridine (BrdU)-labeled PMNs and (B) monocytes after operations with cardiopulmonary bypass (CPB) (solid line) or without CPB (control group: dashed line). Peak of each BrdU-labeled cell appearance after the BrdU injection in CPB group was significantly earlier than in control group. Number of these cells in circulation followed same pattern as percentages. Each value represents mean ± standard error (SE) obtained for 4 to 5 monkeys. *P < 0.05 versus control group.*

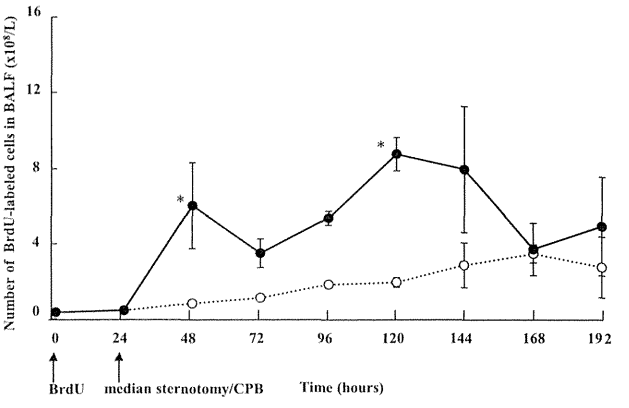


Containing $PMN^{BrdU}$ (%)

| | | | | | | | | |
|---|---|---|---|---|---|---|---|---|
| CPB : | 34.5 | 51.5 | 41.7 | 53.2 | 65.8 | 59.7 | 59.2 | 50.8 |
| Control : | 37.5 | 49.8 | 35.3 | 40.5 | 46.7 | 41 | 38.2 | 39.8 |

*Fig 4. Number of 5-bromo-2′-deoxyuridine (BrdU)-labeled cells in the bronchoalveolar lavage fluid (BALF) after operation with (filled circles, solid line) or without CPB (controls; unfilled circles, dashed line). Recruitment of BrdU-labeled cells to alveolar spaces was accelerated when compared with that of control group, but their peak was delayed (96 hours after CPB). BrdU-labeled PMNs ($PMN^{BrdU}$) at 96 hours after CPB remained majority (65.8%) of labeled cells in alveolar spaces. Each value represents mean ± standard error (SE). *P < 0.05 versus control group.*

show that CPB induced a significant increase in both IL-6 and IL-8 levels in BALF after CPB. These cytokines are thought to be important mediators produced by pulmonary cells such as alveolar macrophages and lung epithelial cells for the production and mobilization of leukocytes from the BM. IL-6 is considered an important multifunctional cytokine involved in the regulation of a variety of cellular responses, including the induction of acute-phase protein synthesis, lymphocyte activation, and hematopoiesis. IL-8 is known as a potent activator that stimulates the BM to release leukocytes [12]. Therefore, we suspect that the release of a combination of inflammatory mediators from pulmonary cells, which is induced by the initial accumulation of activated circulating leukocytes during CPB, is responsible for the production and release of leukocytes from the BM or the recruitment of these cells to the lungs. The possible mechanisms of leukocyte sequestration after CPB need further investigation.

Our results demonstrate that the calculated transit times of PMNs and monocytes through the BM (143.6 ± 4.5 and 100.9 ± 7.6 hours, respectively) in normal-state monkeys with body weights equivalent to those of human infants were almost equal to the values for humans, especially the BM transit of PMNs (144–312 hours) [5], indicating that this in vivo model is relevant for monitoring the kinetics of BM-derived leukocytes in humans. Another advantage of the primate model is that its cardiopulmonary vascular system is completely analogous to that found in humans undergoing CPB. In the present study, we successfully developed a precise monkey model of CPB, with excellent survival during an uneventful follow-up period (192 hours). Using this model, we quantitatively clarified previous reports that CPB increases the release of PMN and monocytes from the BM into the circulation with an acceleration of their BM transit. Interestingly, although a significant difference was not found when compared with the monkeys who did not undergo operation, even undergoing a sternotomy for CPB (control group) also reduced the transit time of leukocytes through the BM (Table 1), suggesting that just an exploratory thoracotomy in the usual clinical setting could result in a leukocyte response from the BM.

This study has several limitations. Our established monkey model did represent pulmonary ischemic-reperfusion associated with CPB but not cardiac ischemia that could have a possible effect on the inflammation. Moreover, the model did not always represent a condition of post-CPB lung injury characterized by excessive interstitial pulmonary edema and subsequent abnormal gas exchange. Arterial blood gas analysis (data not shown) after the operation tended to show lower arterial partial oxygen tension in the CPB group compared with the control group; these levels recovered to become equal within 3 days after the operation. Because our design here required a protocol in which the monkeys could survive longer than 1 week after CPB to allow us to take

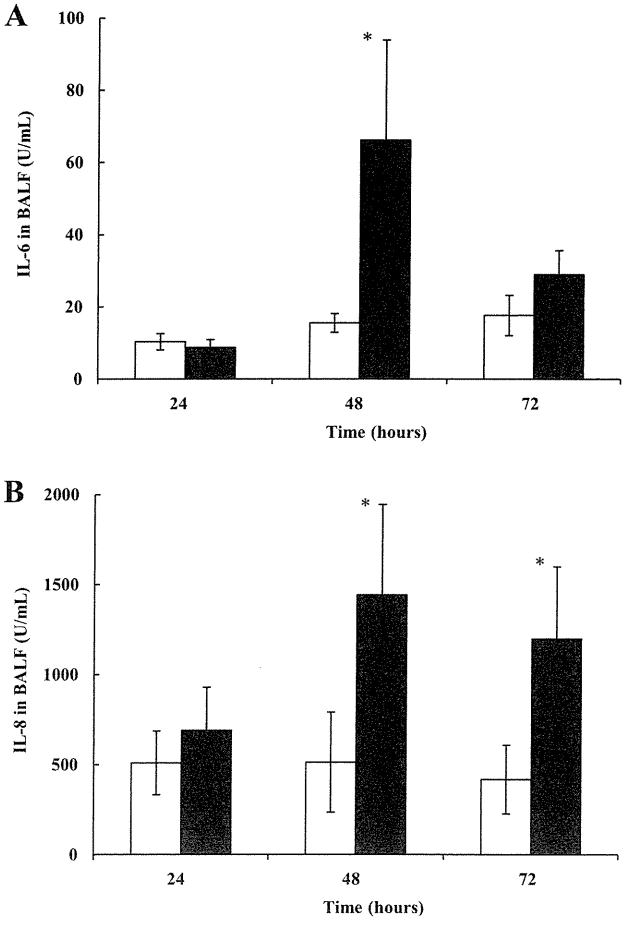


*Fig 5. (A) Interleukin (IL)-6 and (B) IL-8 levels in bronchoalveolar lavage fluid (BALF) after operation with (filled bars) or without CPB (control group; unfilled bars). Surgical procedure was performed at time 24 hours. IL-6 increased significantly at 48 hours, as did IL-8 at 48 hours and also at 72 hours in CPB group compared with control group. Each value represents mean ± standard error (SE). *P < 0.05 versus control group.*

repeated blood samples from the same monkey and thus calculate the transit time of leukocytes through the BM, we could not obtain the lung tissues during the protocol to evaluate lung injury in our model. In addition, the temporal relationship of PMN and monocyte recruitment into the alveolar spaces of the lungs associated with CPB remains unclear. Because our protocol unfortunately could not avoid the problem of labeled monocytes being added by release from the BM or division in the lung, we could not ascertain whether BM-derived monocyte recruitment associated with CPB actually occurs.

In summary, we confirmed that CPB accelerates the release of PMNs and monocytes from the BM and showed their delayed recruitment to the lungs in a monkey model that is relevant for humans. We postulate that the behavior of BM-derived leukocytes after CPB, rather than of circulating leukocytes, plays an important role in the pathogenesis of lung injury after CPB and is a part of a whole-body inflammatory reaction.

This work was supported by Grants-in-Aid for Scientific Research (YG and YH) from the Japan Society for the Promotion of Science. The authors thank Yuko Katakai and Hiromi Ogawa, Tsukuba Primate Research Center, for technical support; Hideto Takahashi, Faculty of Medicine, University of Tsukuba, for statistical analysis; and Flaminia Miyamasu, Medical English Communications Center, University of Tsukuba, for grammatical review of this article.

## References

1. Matsuzaki K, Hiramatsu Y, Homma S, Sato S, Shigeta O, Sakakibara Y. Sivelestat reduces inflammatory mediators and preserves neutrophil deformability during simulated extracorporeal circulation. Ann Thorac Surg 2005;80:611–7.
2. Sato Y, Hiramatsu Y, Homma S, et al. Phosphodiesterase type 4 inhibitor rolipram inhibits activation of monocytes during extracorporeal circulation. J Thorac Cardiovasc Surg 2005;130:346–50.
3. Apostolakis E, Filos KS, Koletsis E, Dougenis D. Lung dysfunction following cardiopulmonary bypass. J Card Surg 2010;25:47–55.
4. Asimakopoulos G, Smith PL, Ratnatunga CP, Taylor KM. Lung injury and acute respiratory distress syndrome after cardiopulmonary bypass. Ann Thorac Surg 1999;68:1107–15.
5. Fliedner TM, Cronkite EP, Killmann SA, Bond VP. Granulocytopoiesis. II. Emergence and pattern of labeling of neutrophilic granulocytes in humans. Blood 1964;24:683–700.
6. Goto Y, Hogg JC, Suwa T, Quinlan KB, van Eeden SF. A novel method to quantify the turnover and release of monocytes from the bone marrow using the thymidine analog 5′-bromo-2′-deoxyuridine. Am J Physiol Cell Physiol 2003;285:C253–9.
7. Honjo S. The Japanese Tsukuba Primate Center for Medical Science (TPC): an outline. J Med Primatol 1985;14:75–89.
8. Primate Society of Japan. Guiding principles for animal experiments using nonhuman primates. Primate Res 1986;2:111–3.
9. van Eeden SF, Kitagawa Y, Klut ME, Lawrence E, Hogg JC. Polymorphonuclear leukocytes released from the bone marrow preferentially sequester in lung microvessels. Microcirculation 1997;4:369–80.
10. Goto Y, Hogg JC, Whalen B, Shih CH, Ishii H, Van Eeden SF. Monocyte recruitment into the lungs in pneumococcal pneumonia. Am J Respir Cell Mol Biol 2004;30:620–6.
11. Grunenfelder J, Umbehr M, Plass A, et al. Genetic polymorphisms of apolipoprotein e4 and tumor necrosis factor beta as predisposing factors for increased inflammatory cytokines after cardiopulmonary bypass. J Thorac Cardiovasc Surg 2004;128:92–7.
12. Finn A, Naik S, Klein N, Levinsky RJ, Strobel S, Elliott M. Interleukin-8 release and neutrophil degranulation after pediatric cardiopulmonary bypass. J Thorac Cardiovasc Surg 1993;105:234–41.

*Genes* **2014**, *5*, 1095-1114; doi:10.3390/genes5041095

OPEN ACCESS

*genes*

ISSN 2073-4425

www.mdpi.com/journal/genes

*Article*

# Altered Actions of Memantine and NMDA-Induced Currents in a New *Grid2*-Deleted Mouse Line

**Ayako Kumagai [1,†], Akira Fujita [2,†], Tomoki Yokoyama [2,†], Yuki Nonobe [2,†], Yasuhiro Hasaba [2,†], Tsutomu Sasaki [3], Yumi Itoh [1], Minako Koura [4], Osamu Suzuki [4], Shigeki Adachi [5], Haruko Ryo [5], Arihiro Kohara [6], Lokesh P. Tripathi [7], Masato Sanosaka [1], Toshiki Fukushima [2], Hiroyuki Takahashi [2], Kazuo Kitagawa [3], Yasuo Nagaoka [8], Hidehisa Kawahara [8], Kenji Mizuguchi [7], Taisei Nomura [5], Junichiro Matsuda [4], Toshihide Tabata [2,*] and Hiroshi Takemori [1,*]**

[1] Laboratory of Cell Signaling and Metabolic Disease, National Institute of Biomedical Innovation, Saito-Asagi, Ibaraki, Osaka 567-0085, Japan; E-Mails: a-kumagai@nibio.go.jp (A.K.); y-itou@nibio.go.jp (Y.I.); m-sanosaka@nibio.go.jp (M.S.)

[2] Laboratory for Neural Information Technology, Graduate School of Science and Engineering, University of Toyama, Toyama 930-8555, Japan; E-Mails: fujita0153@gmail.com (A.F.); m1371119@ems.u-toyama.ac.jp (T.Y.); weather4519@gmail.com (Y.N.); takegoshiyoshihiro45@gmail.com (Y.H.); fookun3@gmail.com (T.F.); m1471114@ems.u-toyama.ac.jp (H.T.)

[3] Department of Neurology, Osaka University Graduate School of Medicine, Osaka 565-0871, Japan; E-Mails: sasaki@medone.med.osaka-u.ac.jp (T.S.); kitagawa@neurol.med.osaka-u.ac.jp (K.K.)

[4] Laboratory of Animal Models for Human Diseases, National Institute of Biomedical Innovation, Saito-Asagi, Ibaraki, Osaka 567-0085, Japan; E-Mails: koura@nibio.go.jp (M.K.); osuzuki@nibio.go.jp (O.S.); jmatsuda@nibio.go.jp (J.M.)

[5] Nomura Project, National Institute of Biomedical Innovation, Saito-Asagi, Ibaraki, Osaka 567-0085, Japan; E-Mails: sadachi@nibio.go.jp (S.A.); hryo@nibio.go.jp (H.R.); n5nomura@nibio.go.jp (T.N.)

[6] Laboratory of Cell Cultures, National Institute of Biomedical Innovation, Saito-Asagi, Ibaraki, Osaka 567-0085, Japan; E-Mail: kohara@nibio.go.jp

[7] Laboratory of Bioinformatics, National Institute of Biomedical Innovation, Saito-Asagi, Ibaraki, Osaka 567-0085, Japan; E-Mails: lokesh@nibio.go.jp (L.P.T.); kenji@nibio.go.jp (K.M.)

[8] Department of Life Science and Biotechnology, Kansai University, Suita, Osaka 564-8680, Japan; E-Mails: t010034@kansai-u.ac.jp (Y.N.); t912436@kansai-u.ac.jp (H.K.)

† These authors contributed equally to this work.

* Authors to whom correspondence should be addressed; E-Mails: takemori@nibio.go.jp (H.T.); ttabata@eng.u-toyama.ac.jp (T.T.); Tel.: +81-72-641-9834 (H.T.); Fax: +81-72-641-9836 (H.T.); Tel.: +81-76-445-6742 (T.T.); Fax: +81-76-445-6703 (T.T.).

*Received: 14 October 2014; in revised form: 12 November 2014 / Accepted: 2 December 2014 / Published: 11 December 2014*

**Abstract:** Memantine is a non-competitive antagonist of the *N*-methyl-D-aspartate (NMDA) receptor, and is an approved drug for the treatment of moderate-to-severe Alzheimer's disease. We identified a mouse strain with a naturally occurring mutation and an ataxic phenotype that presents with severe leg cramps. To investigate the phenotypes of these mutant mice, we screened several phenotype-modulating drugs and found that memantine (10 mg/kg) disrupted the sense of balance in the mutants. Moreover, the mutant mice showed an attenuated optokinetic response (OKR) and impaired OKR learning, which was also observed in wild-type mice treated with memantine. Microsatellite analyses indicated that the *Grid2* gene-deletion is responsible for these phenotypes. Patch-clamp analysis showed a relatively small change in NMDA-dependent current in cultured granule cells from *Grid2* gene-deleted mice, suggesting that GRID2 is important for correct NMDA receptor function. In general, NMDA receptors are activated after the activation of non-NMDA receptors, such as AMPA receptors, and AMPA receptor dysregulation also occurs in *Grid2* mutant mice. Indeed, the AMPA treatment enhanced memantine susceptibility in wild-type mice, which was indicated by balance sense and OKR impairments. The present study explores a new role for GRID2 and highlights the adverse effects of memantine in different genetic backgrounds.

**Keywords:** GRID2; GluRδ2; memantine; NMDA receptor; cerebellum

## 1. Introduction

Memantine (3,5-dimethyl-1-adamantanamine) is an approved drug in the treatment of moderate-to-severe Alzheimer's disease (AD). $Ca^{2+}$-mediated excitotoxicity in neurons is one proposed mechanism of AD, and the *N*-methyl-D-aspartate (NMDA) receptor is one of the major receptor channels responsible for glutamate-induced $Ca^{2+}$ influx. Memantine binds and non-competitively inhibits NMDA receptors, which subsequently protects neurons from glutamate-induced excitotoxicity [1,2].

Glutamate is essential for excitatory synaptic transmission mediated by ionotropic glutamate receptors, which include NMDA receptors and non-NMDA receptors, α-amino-3-hydroxy-5-methyl-4-isoxazolepropionic acid (AMPA) and kainate receptors [3]. NMDA receptor activation is dependent on the membrane potential that is evoked by non-NMDA receptor function [4]. Under pathological conditions, the voltage-dependent regulation of NMDA receptors is believed to be impaired, and memantine is thought to alleviate excitotoxicity by the unregulated NMDA receptor.

Unlike memantine, other NMDA receptor antagonists, such as MK-801 [5], are considered neurotoxins because they inhibit normal excitotoxic neurotransmission as well as pathological physiological neurotransmission. Although memantine is considered a relatively safe drug, some adverse effects, such as dizziness [6], have been reported. Such adverse effects are likely to result from individual differences among patients, especially in their genetic backgrounds. However, the causes of adverse effects to memantine have not yet been clarified.

The glutamate receptor ionotropic delta 2 (GRID2, also known as GluRδ2) is abundantly expressed in cerebellar Purkinje cells, and shares sequence homology with other glutamate receptors. Despite its name and these homologies, GRID2 does not bind glutamate or other glutamate analogs [7–9]. Mice with an impaired *Grid2* gene exhibit a broad range of phenotypes, such as cerebellar ataxia, poor motor learning, and memory dysfunction. In addition to the known phenotypes in mice, new phenotypes presumably involving NMDA receptor dysfunction or memantine effects, such as nystagmus (in frogs) [10], oculomotor apraxia (in cats) [11,12], dementia (in humans) [13,14], have been observed in human patients with *GRID2* gene deletions [15–18]. However, there is not sufficient evidence to ascribe these complex symptoms in human patients to *GRID2* gene deletions.

Here, we report a new deletion in the mouse *Grid2* gene that is accompanied by ataxia. Administration of memantine led to impaired balance in ataxic mice, and the mutant mice showed deficits in the optokinetic response (OKR) and its learning. These optokinetic impairments were also sensitive to memantine. In addition, only a small population of cultured granule cells isolated from the mutant mice showed memantine-sensitive NMDA-induced currents. These phenomena were mimicked in wild-type (WT) mice following co-treatment with memantine and AMPA.

## 2. Results

### *2.1. The Hereditary Ataxic Mouse is Sensitive to Memantine*

Two ataxic (male and female) mice appeared spontaneously in the same litter from a mating pair of hetero mice with the knockout (KO) allele for Salt-Inducible Kinase 3 (*Sik3*: $Sik3^{tm1Htake/+}$) [19] on a C57BL/6J (B6) genetic background. The male was $Sik3^{+/-}$, but the female was $Sik3^{+/+}$. Because these ataxic mice failed to produce offspring by natural mating, we performed *in vitro* fertilization (IVF) using these ataxic mice and confirmed the heredity of the phenotype. To expound the mouse population, the original sperm of the ataxic male was also used for other IVF with the oocyte of normal B6 female, and offspring with the ataxic phenotype were obtained at the F2 generation (numbers of normal male, ataxic male, normal female, and ataxic female were 4, 1, 9, and 2, respectively), suggesting a recessively-inherited phenotype. Despite showing normal forelimb movements, the mutant offspring were characterized by a short-stepped gait and frequent falls due to suspected leg cramps (Figure 1A).

To examine whether the phenotype was caused by a neurogenic disorder, neuropharmacological compounds were tested in the normal and mutant mice. Because anesthesia (1% isoflurane) [20] alleviated leg cramps in the mutant mice, we first selected anticonvulsant drugs including gamma-aminobutyric acid (GABA) receptor activators and NMDA receptor antagonists (Table 1). The GABA-A receptor activators felbamate and nitrazepam failed to modulate the phenotypes in the mutant mice. Whereas, memantine (10 mg/kg), an NMDA and $5HT_3$ receptor antagonist which is also

reported to exert agonistic actions for the dopamine D2 receptor [21,22], impaired balance in the mutant mice, but not normal mice (Figure 1B and Supplementary Movie 1). Movement traces of the mice (Figure 1C) confirmed that 10 mg/kg memantine had no significant effect on walking in normal mice.

**Figure 1.** Isolation of ataxic mice with memantine susceptibility. (**A**) A mouse (6-month-old female) that exhibited an ataxic phenotype with rigid hind limbs. The phenotype became more severe with age; (**B**) Footprint analyses 10 min after memantine treatment (10 mg/kg, 12-week-old male). The soles of the hind limbs were labeled with India ink for a mouse that walked freely on paper. Rollover by the mutant mouse after memantine treatment is shown (lower right); (**C**) Monitoring mice walking after memantine treatment (10 mg/kg, 12-week-old male). The position of the mouse's head was tracked (left), and the walking distance was recorded for 5 min (right; expressed as the mean and SD; n = 6). * $p < 0.05$, ** $p < 0.01$.

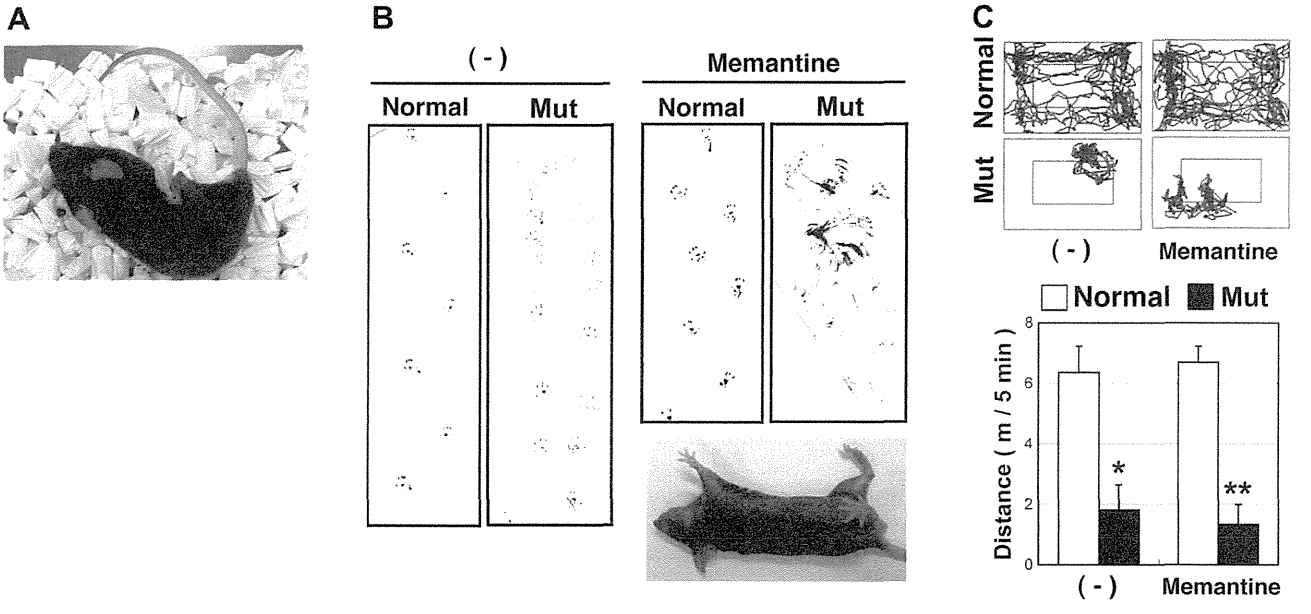


Next, we tested other NMDA receptor modulators. Similar to memantine, the NMDA receptor antagonist MK-801 (10 mg/kg) led to balance disturbances in the mutant mice. However, the normal mice also showed balance disturbances at this dose (Table 1). (*R*)-CPP also produced balance disturbances only in the mutant mice (Supplementary Movie 2), whereas ifenprodil, Ro25-6981, or the AMPA receptor antagonist DNQX did not produce balance disturbances in the mutant or normal mice. However, slower movements were observed in mutant mice following administration of DL-AP7.

Because serotonin reuptake inhibitors are used to treat vertigo [23], and the $5HT_3$ antagonist ondansetron causes headache and dizziness [24], we examined whether ondansetron affected the mutant mice. Both mutant and normal mice showed decreased activity with ondansetron (10 mg/kg; Supplementary Movie 3), but no effect that was specific to mutant mice was observed. Moreover, enhanced cholinergic signaling following donepezil treatment [21] and activation of dopamine signals by L-Dopa [21,22] had no significant effect on behavior in both normal and mutant mice (Table 1). These results suggest that, in addition to the ataxic phenotype, the mutant mice were characterized by enhanced memantine susceptibility, which was probably due to impaired NMDA receptor functions. The inconsistency in the efficacy of NMDA receptor antagonists on balance disturbance might result

from differences in NMDA receptor subunit subtype-specificity and/or effective dose among the antagonists; 10 mg/kg and 10–20 mg/kg might be the threshold doses to affect balance in the mutant mice for memantine and (*R*)-CPP, respectively.

**Table 1.** Pharmacological effectors on mutant mice phenotypes.

| Chemical | Category | Dose (mg/kg) | Number of Mice | Movement of Normal Mice | Movement of Mutant Mice |
|---|---|---|---|---|---|
| Memantine | NMDA-R antagonist | 2 | 2 | NS | NS |
| | | 10 | 2 | NS | Balance loss |
| MK-801 | NMDA-R antagonist | 2 | 2 | NS | NS |
| | | 10 | 3 | Balance loss | Balance loss |
| DL-AP7 | NMDA-R antagonist | 30 | 2 | NS | Slow movement |
| (R)-CPP | NMDA-R antagonist (NR2A antagonist) | 10 | 4 | NS | Balance loss * |
| | | 20 | 2 | NS | Balance loss |
| Ro25-6981 | NMDA-R antagonist | 2 | 3 | NS | NS |
| | | 10 | 3 | NS | NS |
| Ifenprodil | NMDA-R antagonist (NR2B antagonist) | 2 | 3 | NS | NS |
| | | 10 | 3 | NS | NS |
| Felbamate | NR2B antagonist GABA-R activator | 30 | 2 | NS | NS |
| Nitrazepam | GABA-R activator | 30 | 2 | NS | NS |
| Isoflurane | GABA-R activator | 1% in air | 2 | Slip | Slip |
| DNQX | AMPA/Kainate receptor antagonist | 2 | 3 | NS | NS |
| | | 10 | 3 | NS | NS |
| Ondansetron | 5-HT3 antagonist | 5 | 2 | NS | NS |
| | | 10 | 2 | Not move | Not move |
| Donepezil | acetylcholinesterase inhibitor | 10 | 3 | NS | NS |
| L-Dopa | Dopamine precursor | 20 | 3 | NS | NS |

NS: No significant effect was observed. *: 2 mice.

### *2.2. Impaired OKR and Learning in the Ataxic Mice*

Gait disorders are a common pathology in patients with spinocerebellar degeneration, and are sometimes accompanied by vertigo resulting from oculomotor dysfunction [25,26]. Memantine also affects oculomotor functions in patients with cerebellar ataxia [27]. To examine whether our mutant mice also had oculomotor impairments, we measured the OKR and OKR adaptation, a form of cerebellum-dependent learning [28,29], and used the results from these assays to quantify memantine susceptibility (Supplementary Figure S1).

Normal and mutant mice were subjected to the OKR assay and horizontal visual pattern oscillations were given (Figure 2A). The normal mice could track the stimulus screen, whereas the mutant mice could not. Memantine (10 mg/kg) significantly lowered the overall OKR gain throughout a 1 h session in normal mice while the OKR in mutant mice was completely abolished (Figure 2B).

To evaluate OKR adaptation, the mean OKR gain was plotted for each 10-min interval (Figure 2C). Saline-injected normal mice (control) exhibited a time-dependent increase in the OKR gain, but no gain increase was observed in the mutant or the memantine-treated normal mice.

**Figure 2.** The optokinetic response (OKR) and its susceptibility to memantine. (**A**) The OKR of normal and mutant mice after intraperitoneal injection of saline (control) or memantine-containing saline (10 mg/kg). Measurements commenced 10 min after injection. Representative OKRs from normal and mutant mice are shown. The relative pupil azimuth is plotted against time. Each trace indicates the average over each 10-min period of a 1-h measurement session. Screen, movement of the stimulus screen; (**B**) Overall OKR gain throughout the 1-h session with or without memantine. Dots and error bars, mean ± SD; n = 5 for each data point. * $p < 0.05$, ** $p < 0.01$, and **** $p < 0.0001$, multivariate ANOVA. The overall OKR gain was calculated by averaging the OKR gains for all 10-min periods in a single 1-h session (see panel C); (**C**) Time course of the mean OKR gain for normal (n = 5) and mutant (n = 5) mice. Each dot indicates the average over a 10-min period of a 1-h measurement session. Error bars indicate ±SD. **** $p < 0.0001$ *vs.* the control for time × drug interaction, repeated measures ANOVA.

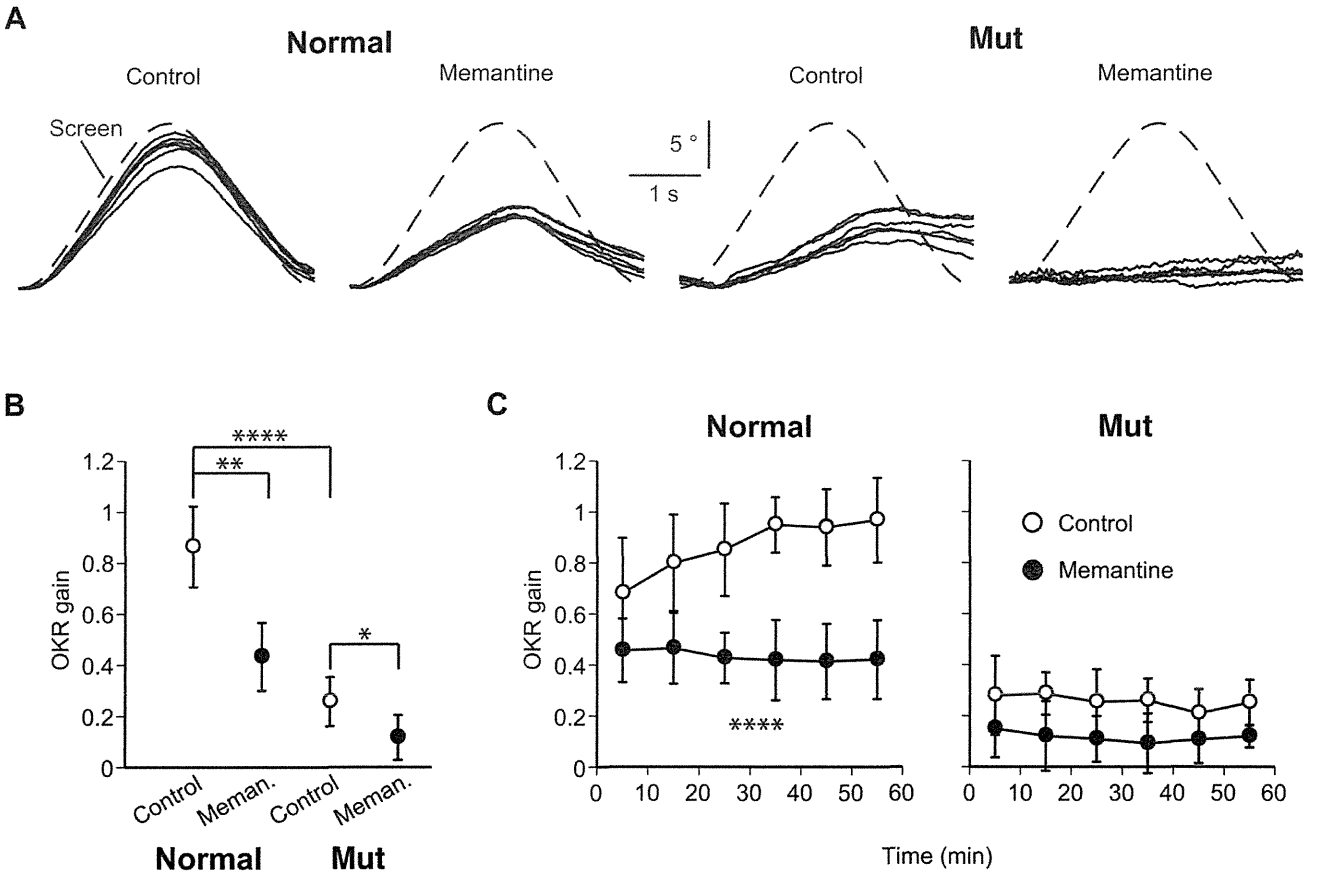

### *2.3. Microsatellite Analysis in the Ataxic Mice*

Because the pharmacological analyses were unable to predict the gene responsible for the ataxic phenotype, we performed a microsatellite analysis to identify the gene. Sperm were isolated from an ataxic mouse (N0: C57BL/6J[B6], B6/B6) and used to perform IVF with oocytes from C3H/HeN (C3) mice (normal: C3/C3). Oocytes were prepared from the N1 female (B6/C3 hetero-mice) and used for a second round of IVF using the original sperm from the N0 (B6/B6) ataxic mice, which produced 137 N2 mice (75 non-ataxic (the responsible genomic-region should be B6/C3) and 62 ataxic (the responsible genomic-region should be B6/B6)). Using 60 microsatellite markers and DNA from eight N2 non-ataxic mice, we screened heterogenic-regions composed of both B6 and C3 chromosomes. We observed that D6Mit149 (Chromosome 6, 48.93 cM) was amplified as the heterogenic-type in all eight mice. Next, we analyzed other markers near D6Mit149 using DNA from 70 mice (Figure 3A) and narrowed the responsible region to 27.3–32.2 cM (D6Mit384–D6Mit243), which was also associated with the phenotype of enhanced memantine susceptibility.

**Figure 3.** Identification of the responsible gene. (**A**) Microsatellite analyses of N2 mice. B6, parental allele of the ataxic mouse (C56BL/6J); C3, WT allele of C3H/HeN. N2 mice were produced following *in vitro* fertilization with oocytes from hetero N1 (B6/C3) and sperm from the original N0 ataxic B6 (B6/B6). Markers are described in the Experimental Section. Normal and Mut indicate mice with or without the ataxic phenotype, respectively. The *Grid2* gene is located 29.77 cM in chromosome 6; (**B**) The full-length open reading frame ORF of *Grid2* was amplified from cDNA prepared from the cerebellum of WT and Mut mice; (**C**) Western blotting for GRID2; (**D**) A diagram showing break points in the *Grid2* gene of ataxic mice; (**E**) Putative protein sequence of GRID2 in *Grid2*$^{Htake/Htake}$ mice is predicted from diagram D and the direct ORF sequence.

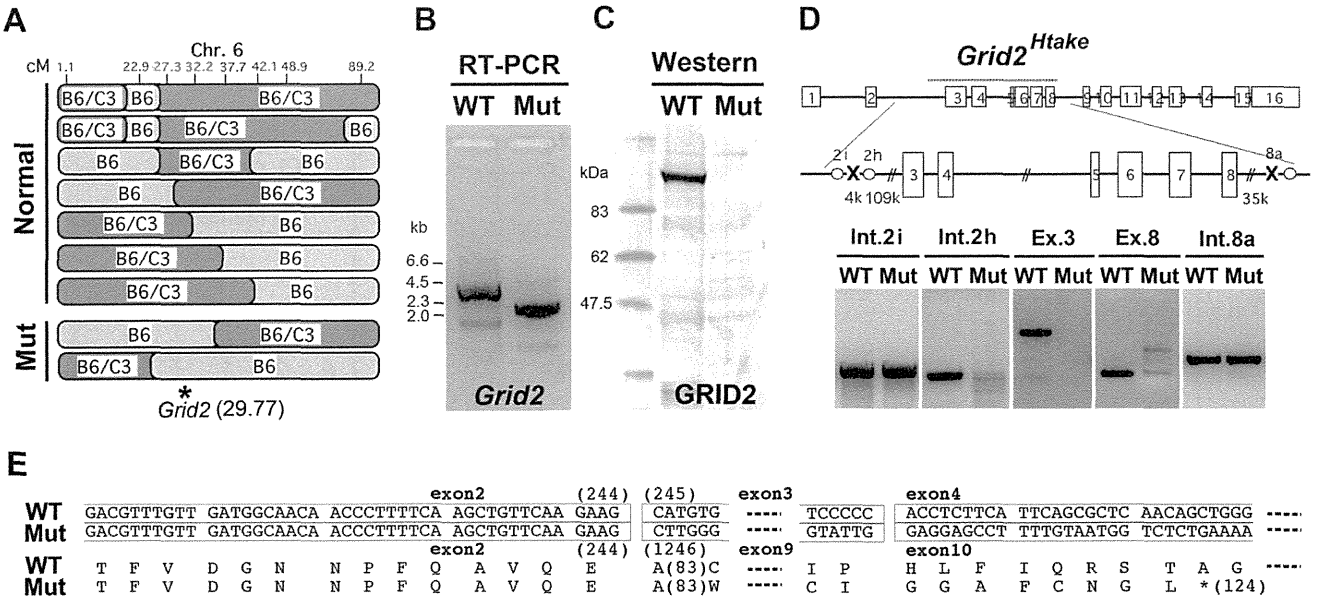


When we searched for genes that have known associations with ataxic phenotypes, we noticed the *Grid2* gene at 29.77 cM [30]. To determine whether this gene was responsible for the observed

phenotype, the *Grid2* open reading frame (ORF) was amplified from cDNA prepared from the cerebellum. As shown in Figure 3B, the *Grid2* ORF was approximately 1 kb shorter in the mutant mice than in the WT mice. In addition, western blotting for GRID2 revealed that this protein was absent from the mutant cerebellum (Figure 3C).

Direct sequencing of the mutant ORF suggested that the region from exon 3 to exon 8 might be deleted, which is the longest deletion reported in *Grid2* mutant mice [31]. Chromosome walking (Figure 3D) identified the break points 110 kb upstream from exon 3 and 30 kb downstream from exon 8, which yielded a truncated GRID2 protein similar to that in the $Grid2^{trp/trp}$, $Grid2^{ho8J/ho8J}$, and $Grid2^{ho13J/ho13J}$ mutants, but with different flanking peptides (Figure 3E). Our laboratory code for mutant mouse lines is Htake, thus the mutant allele is named $Grid2^{Htake}$.

### *2.4. Altered Sensitivity to NMDA in Cultured Granule Cells of $Grid2^{Htake/Htake}$ Mice*

GRID2 is highly expressed in Purkinje cells, and disruption of GRID2 signaling impairs Purkinje cell functions. However, little or no expression of functional NMDA receptors in Purkinje cells of the adult cerebellum has been reported [32]. Thus, it is possible that *Grid2* gene deletion influences cerebellar function by affecting NMDA receptors on granule cells. We examined whether $Grid2^{Htake/Htake}$ mice possessed memantine-sensitive NMDA receptors on cerebellar granule cells, using granule cell-enriched (Purkinje cell-free) primary cultures from P2 mice. Quantitative PCR (Figure 4A) and western blot analyses (Figure 4B) showed that cultured granule cells expressed low, but detectable, levels of *Grid2* mRNA and GRID2 protein. No significant difference in NMDAR1 protein level was observed between the cultures derived from normal and $Grid2^{Htake/Htake}$ mice, which was consistent with the result of mRNA (microarray) analyses (Supplementary Table S1).

We have to note, however, that no significant interaction between GRID2 protein and NMDAR1 protein in the total cerebella or cultured granule cell lysate was observed (Supplementary Figure S2), despite the presence of PKC gamma binding to GRID2 protein [33].

Next, we monitored NMDA-induced currents in cultured granule cells using a whole-cell voltage-clamp technique. At cell densities as low as 1.25 million cells/mL and a holding potential of −90 mV, granule cells from both WT and mutant mice showed no baseline activity (Figure 4C). In the absence of memantine (before memantine), NMDA (20 μM, 2 s) induced inward currents that were larger in WT cells than in mutant cells. Furthermore, NMDA-induced currents were reduced in the presence of memantine (after memantine: 10 μM, 30 s). However, the magnitude of the memantine-dependent suppression of the NMDA-induced currents varied in the individual cells.

To accurately categorize the memantine-sensitive NMDA-induced currents, we divided the cells into two categories based on the ability of memantine to reduce the charge density of NMDA-induced currents by more than 75%. According to this classification, 51.9% of WT cells and only 21.4% of mutant cells were categorized as memantine-sensitive (Figure 4D). Moreover, the classification (only open circles) revealed that the values of charge density from the mutant cells fell into a lower range, which produced a significant difference in the variance of the charge density between the WT and mutant groups (Figure 4E). These results suggest that mutant mice might possess a poor variation of NMDA receptor with reduced function on their granule cell population.

**Figure 4.** NMDA-responsiveness of cultured cerebellar granule cells. (**A**) The raw data for quantitative PCR analyses and normalized levels (inset: n = 4) of *Gird2* mRNA are indicated. Total RNA was prepared from total cerebellum, 2-week-cultured cerebellar granule cells from neonates (P2), B16F10 melanoma cells (non-neuronal negative control); (**B**) Western blotting was performed using WT and *Grid2*$^{Htake/Htake}$ (Mut) total cerebella or cultured granule cells. There is no significant difference in NMDAR1 protein level; (**C**) Whole-cell current responses of cultured granule cells derived from WT and Mut mice to local application of NMDA (20 μM, 2 s) before and after treatment with memantine (10 μM, 30 s). Representative currents recorded from single WT and Mut cells. Arrowheads indicate artifacts due to the opening and closure of the electromagnetic valve controlling delivery of NMDA-containing saline; (**D**) The examined cells were categorized into two groups by memantine susceptibility, and their populations are represented as % fractions. When more than 75% of NMDA-induced inward current was suppressed by memantine, the cells were categorized into the memantine-sensitive group (white area). Cells that experienced reduced inward current suppression after memantine treatment, or no significant inward current were categorized into the memantine-insensitive group (black area). * $p = 0.0178$, likelihood ratio test (WT, n = 27; Mut, n = 28); (**E**) Distribution of the total charge density of NMDA-induced inward currents. Open circles (white) and closed triangles (black) indicate the data from cells categorized as D. The magnitude of the total data (white and black) was not significantly different between the WT and mutant cells (medians, 1.01 and 0.64 pC/pF, respectively). However, in a comparison of the data from the memantine-sensitive cells (white), there was a significant difference in variance between the WT and mutant cells (* $p = 0.0120$, Brown-Forsythe test).